buildings

MDPI

Article

Novel Multi-Vibration Resonator with Wide Low-Frequency Bandgap for Rayleigh Waves Attenuation

Hui Jiang [1], Chunfeng Zhao [1,2,*], Yingjie Chen [1,*] and Jian Liu [1]

[1] College of Hydraulic and Civil Engineering, Xinjiang Agricultural University, Ürümqi 830052, China; 320222317@xjau.edu.cn (H.J.); xjliujian117@xjau.edu.cn (J.L.)
[2] College of Civil Engineering, Hefei University of Technology, Hefei 230009, China
* Correspondence: zhaowindy@hfut.edu.cn (C.Z.); chenyj2021@xjau.edu.cn (Y.C.)

Abstract: Rayleigh waves are vertically elliptical surface waves traveling along the ground surface, which have been demonstrated to pose potential damage to buildings. However, traditional seismic barriers have limitations of high-frequency narrow bandgap or larger volume, which have constraints on the application in practical infrastructures. Thus, a new type seismic metamaterial needs to be further investigated to generate wide low-frequency bandgaps. Firstly, a resonator with a three-vibrator is proposed to effectively attenuate the Rayleigh waves. The attenuation characteristics of the resonator are investigated through theoretical and finite element methods, respectively. The theoretical formulas of the three-vibrator resonator are established based on the local resonance and mass-spring theories, which can generate wide low-frequency bandgaps. Subsequently, the frequency bandgaps of the resonator are calculated by the finite element software COMSOL5.6 based on the theoretical model and Floquet–Bloch theory with a wide ultra-low-frequency bandgap in 4.68–22.01 Hz. Finally, the transmission spectrum and time history analysis are used to analyze the influences of soil and material damping on the attenuation effect of resonators. The results indicate that the resonator can generate wide low-frequency bandgaps from 4.68 Hz to 22.01 Hz and the 10-cycle resonators could effectively attenuate Raleigh waves. Furthermore, the soil damping can effectively attenuate seismic waves in a band from 1.96 Hz to 20 Hz, whereas the material of the resonator has little effect on the propagation of the seismic waves. These results show that this resonator can be used to mitigate Rayleigh waves and provide a reference for the design of surface waves barrier structures.

Keywords: local resonance; Rayleigh waves; bandgap; vibration isolation; ultra-low frequency; transmission spectrum; time history analysis

check for updates

Citation: Jiang, H.; Zhao, C.; Chen, Y.; Liu, J. Novel Multi-Vibration Resonator with Wide Low-Frequency Bandgap for Rayleigh Waves Attenuation. *Buildings* **2024**, *14*, 2591. https://doi.org/10.3390/buildings14092591

Academic Editor: Paulo Amado-Mendes

Received: 2 July 2024
Revised: 12 August 2024
Accepted: 20 August 2024
Published: 23 August 2024

Copyright: © 2024 by the authors. Licensee MDPI, Basel, Switzerland. This article is an open access article distributed under the terms and conditions of the Creative Commons Attribution (CC BY) license (https://creativecommons.org/licenses/by/4.0/).

1. Introduction

Earthquakes are one of the most hazardous natural disasters in the world, which release seismic energy through seismic waves and pose a huge hazard to buildings [1]. The seismic waves are combined with surface waves and body waves; Rayleigh waves are vertically elliptical surface waves traveling along the ground surface, which has been demonstrated to pose potential damage to buildings. Simultaneously, the surface wave barriers periodically arranged around the building can protect buildings by attenuating the effects of Rayleigh surface waves.

In recent years, scholars have conducted numerous research on seismic metamaterial surface waves barriers using phononic crystals [2–6]. Surface waves barriers can be classified into two types based on the mechanisms of bandgap generation: Bragg scattering [4,7] and local resonance [8–13]. Bragg scattering type barriers can generate one wide bandgap, effectively attenuating most frequencies within 0–20 Hz. Muhammad et al. [14] designed two 2D columnar barriers with lengths of 12.5 m and calculated the bandgap for both single and multilayered soils. The results showed that the barriers can attenuate surface waves in

both types of soils, offering insights for soil conditions in practical implementation. Witarto et al. [15] analyzed a 3D square cube buried in soil and discovered that a square cube with a period constant of 1 m can generate an elastic waves bandgap from 18.44 Hz to 27.09 Hz. Liu et al. [16] designed a continuous wall that was partially buried underground, which can attenuate elastic waves in the ranges of 6.2–8.8 Hz and 15.1–20 Hz. The attenuation effect of barriers with a positive gradient was better than that of a periodic arrangement, which offers a new method of barrier arrangement. Wang et al. [17] conducted numerical simulations and scaling tests on both the petal-shaped-filled barriers and ordinary square-filled barriers. The results showed that the petal-shaped-filled barriers can generate multiple bandgaps in the range of 0–20 Hz and their effect is superior to that of the ordinary square-filled barriers. Numerous studies [18–29] demonstrated that the Bragg scattering barrier effectively attenuates Rayleigh surface waves. However, the sizes of the most Bragg scattering barriers are too large to apply and implement in practical engineering.

Many studies have been conducted on seismic surface wave resonators based on the theory of local resonance. These resonators were much smaller in size compared to Bragg scattering barriers, making them more beneficial for engineering implementation. Liu et al. [30] proposed a local resonance metamaterial composed of rubber wrapped around a lead ball and arranged in squares. This design achieves the goal of controlling a large wavelength using a small size, providing a new idea for the design of seismic surface waves barriers. A resonant meta-wedge [31] was designed to convert surface waves into body waves and to reflect Rayleigh surface waves, and an analytical model was developed to accurately predict the rainbow effect of earthquakes. Some scholars [32–35] calculated the bandgap of local resonant resonators using the finite element method and concluded that these resonators were capable of generating a low-frequency bandgap, which was helpful for attenuating Rayleigh waves. Some references [36–38] theoretically deduced the attenuation properties of resonators and numerically proved that the theoretical model can achieve an efficient low-frequency bandgap. Yan et al. [39] designed a cubic resonator foundation made of three materials and demonstrated that it can effectively attenuate seismic surface waves by theoretical analysis and field experiments. Palermo et al. [40] designed a 2D super-barrier and showed that it can convert surface waves into body waves to achieve the attenuation of Rayleigh waves. The finite element method showed that the metabarrier was able to attenuate surface waves by converting surface waves into body waves. Additionally, a scaling experiment was conducted to verify that the resonator was indeed able to attenuate surface waves.

In recent years, machine learning has been developed and has achieved certain results in various fields. Wang et al. [41] combined the comparative learning pretraining method with the self-supervised pretraining mode to learn the internal features of the image, and the prediction results were remarkable compared with the traditional methods. Purohit and Dave [42] compared six algorithms and suggested that combining self-supervised learning and weakly-supervised learning to form a self-supervised learning model can better analyze labeled and unlabeled datasets and produce more accurate image segmentation models. Gaur et al. [43] used a neural network to calculate the deformation of elastic–plastic structures and derived the stress–strain relationship, which is consistent with the linear theory and shows the accuracy and effectiveness of the method. Liu and Lu [44] used particle swarm optimization and 10-fold cross-validation to analyze the parameters and their predictions matched the experimental results, indicating that the computational framework is useful for parametric analysis of materials. Koy and Colak [45] provided better prediction of data with short-term variations by combining artificial neural network and vector autoregression. A review of the literature on machine learning revealed that it can be applied to the analysis of dispersion curves of resonators. This enables the estimation of the amplitude of vibrations generated by the resonator and the soil under different conditions. Furthermore, machine learning can be used to optimize the parameter design of the resonator and to analyze the elastic dynamics. These will be studied in detail later.

As mentioned above, theoretical calculations indicate that the local resonance resonator can generate ultra-low-frequency elastic waves bandgap with a smaller size compared to the Bragg scattering barrier, which makes it more favorable for engineering applications. However, this research on local resonance type structures is insufficient, especially the single form, such as only two to three materials wrapped into a spherical structure or arranged into a layered structure. Therefore, a new resonator with a three-vibrator is proposed in this study, which can absorb the energy of elastic waves by the internal vibrators of the resonator to attenuate the energy of the elastic waves. Then, fewer studies have been conducted on seismic surface waves in the range of 0–20 Hz. In this study, we focus on the resonator for the most destructive Rayleigh waves, which can be attenuated effectively from the range of 0 Hz to 20 Hz. Therefore, the resonance effectively attenuates the 0–20 Hz seismic surface waves, which extends the research on bandgap generation by local resonance theory.

This study is organized as follows. Section 2 proposes a theoretical model of a resonator with a three-vibrator based on the local resonance theory and establishes the dynamic equilibrium equation. Section 3 introduces the theoretical calculation method of the finite element model. Section 4 calculates the bandgap of the novel resonator and analyzes the mechanism of bandgap. In Section 5, the transmission spectrum is calculated and the displacement modes are analyzed for the mechanism of bandgap. In Section 6, time history analysis is used to verify the bandgap and attenuation effect of the resonator on seismic surface waves. Section 7 analyzes the effect of resonator size parameters on the bandgap range. Section 8 analyzes the effects of soil and material damping on attenuation characteristics for Rayleigh waves. The main conclusions are presented in Section 9.

2. Theoretical Modeling and Development of Equations of Motion

A theoretical model of resonator with three vibrators is proposed based on the local resonance theory [30,31,34], as shown in Figure 1. The model consists of an outer frame and three internal vibrators. The internal vibrators and the outer frame are connected by springs and the resonators are also connected by springs. Moreover, the springs between the resonators represent the propagation of vibration displacement, while the springs between the outer frame and the internal vibrators represent the vibrational displacement of the internal vibrators. The vibrations generated by the internal vibrators are used to absorb the energy of the elastic waves, thus achieving the purpose of attenuating the elastic waves. The parameters of the resonator are shown in Table 1. The materials are all linearly elastic and undamped.

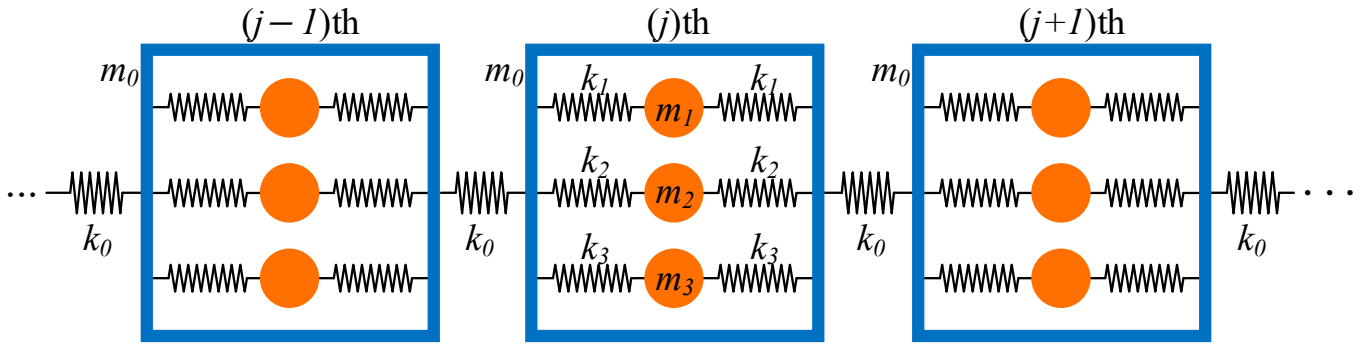


Figure 1. The resonator model.

Table 1. The parameters of the theoretical model.

m_0 (kg)	m_1 (kg)	m_2 (kg)	m_3 (kg)	k_0 (N/m)	k_1 (N/m)	k_2 (N/m)	k_3 (N/m)	A
3	1	1	1	1000	200	200	200	1

The springs are used to connect the outer frame of the resonator to the inner vibrators. When the elastic waves propagate, the energy carried by the elastic waves is transferred to the outer frame m_0 of the resonator through the spring k_0, and then to the internal vibrators m_1, m_2, and m_3 through the springs k_1, k_2, and k_3, respectively, so the internal vibrators can vibrate. The internal vibrators absorb part of the energy of the elastic waves, thus attenuating the elastic waves. On the other hand, damping is an intrinsic property of the material that allows the absorbed energy to be dissipated.

Three theoretical methods can be used to calculate the bandgaps of structure, including plane wave expansion (PWE) [4,46], multiple scattering theory (MST) [10,47–50], and mass-spring theory [37,38,51–54]. The mass-spring theory is the most appropriate method according to the characteristic of the resonators. Thus, as shown in Figure 1, the dynamic equilibrium equations of the resonator can be expressed as follows:

$$\begin{cases} m_0\ddot{u}_0^j + k_0\left(2u_0^j - u_0^{j+1} - u_0^{j-1}\right) \\ +2k_1\left(u_0^j - u_1^j\right) + 2k_2\left(u_0^j - u_2^j\right) + 2k_3\left(u_0^j - u_3^j\right) = 0 \\ m_1\ddot{u}_1^j + 2k_1\left(u_1^j - u_0^j\right) = 0 \\ m_2\ddot{u}_2^j + 2k_2\left(u_2^j - u_0^j\right) = 0 \\ m_3\ddot{u}_3^j + 2k_3\left(u_3^j - u_0^j\right) = 0, \end{cases} \tag{1}$$

where m_0 is mass of the outer frame. m_1, m_2, and m_3 are the internal vibrators, respectively. k_0 is the spring stiffness between the resonators. k_1, k_2, and k_3 are the spring stiffness between the resonator and the internal vibrators, respectively. $\ddot{u}_0^j$ is the displacement of the jth resonator. u_i^j is the displacement of the ith vibrator in the jth resonator. $\ddot{u}_0^j$ and $\ddot{u}_i^j$ are the acceleration of the jth resonator with respect to time and that of the ith vibrator in the jth resonator with respect to time. The displacement function is shown as

$$u_n = U_n e^{\mathrm{i}(ka-\omega t)}, n = 0,\ 1,\ 2,\ 3, \tag{2}$$

where u_0 and u_n are the displacement of the outer frame and the nth internal vibrator, respectively. U_0 and U_n are amplification of the outer frame and the nth internal vibrator, respectively. ω is the circular frequency, t is the time variable, and $\mathrm{i}^2 = -1$. The periodic boundary conditions of the resonator are shown as

$$\begin{cases} u_0^{j-1} = u_0^j e^{-\mathrm{i}ka} \\ u_0^{j+1} = u_0^j e^{\mathrm{i}ka}, \end{cases} \tag{3}$$

where u_0^{j-1} and u_0^{j+1} are the displacement of the $(j-1)$th and $(j+1)$th resonator. k is the wave number and a is the lattice constant. Therefore, the dispersion equation of resonator can be calculated by Equations (1)–(3) and shown as

$$\begin{cases} -\omega^2 m_0 U_0^j + 2k_0(1-\cos(ka))U_0^j \\ +2k_1\left(U_0^j - U_1^j\right) + 2k_2\left(U_0^j - U_2^j\right) + 2k_3\left(U_0^j - U_3^j\right) = 0 \\ -\omega^2 m_1 U_1^j + 2k_1\left(U_1^j - U_0^j\right) = 0 \\ -\omega^2 m_2 U_2^j + 2k_2\left(U_2^j - U_0^j\right) = 0 \\ -\omega^2 m_3 U_3^j + 2k_3\left(U_3^j - U_0^j\right) = 0, \end{cases} \tag{4}$$

Equation (4) can be simplified as

$$\left(\mathbf{\Omega}(k) - \omega^2\mathbf{I}\right)\mathbf{U} = 0, \tag{5}$$

where

$$\mathbf{\Omega}(k) = \begin{bmatrix} 2(1-\cos(ka))\frac{k_0}{m_0} + 2\frac{k_1+k_2+k_3}{m_0} & -2\frac{k_1}{m_0} & -2\frac{k_2}{m_0} & -2\frac{k_3}{m_0} \\ -2\frac{k_1}{m_1} & 2\frac{k_1}{m_1} & 0 & 0 \\ -2\frac{k_2}{m_2} & 0 & 2\frac{k_2}{m_2} & 0 \\ -2\frac{k_3}{m_3} & 0 & 0 & 2\frac{k_3}{m_3} \end{bmatrix}$$

is the fourth-order matrix of the wave vector. **U** is the fourth-order matrix of the displacement. **I** is a fourth-order unit matrix. Therefore, the dispersion curve of resonator can be calculated by Equation (4) and Table 1 and shown in Figure 2. It can be seen from Figure 2 that the theoretical model of the resonator can generate a low-frequency wide bandgap from 2.7 Hz to 4.5 Hz. It can be obtained that the resonator produces one low-frequency wide bandgap when the mass and the spring stiffness of the internal vibrator are the same. Therefore, the theoretical model of the resonator is useful for the attenuation of elastic waves, which provides a theoretical reference for the establishment of the practical model of the resonator.

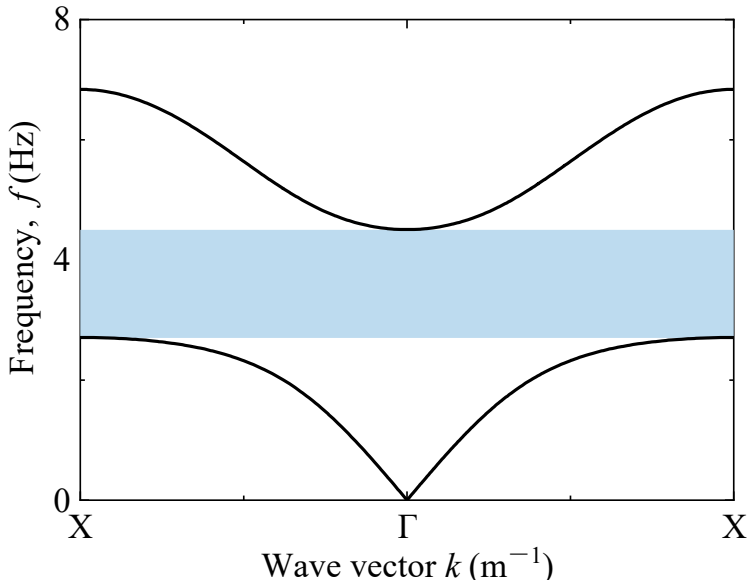


Figure 2. Dispersion curve.

3. Numerical Models

The finite element model of the resonator is established according to the theoretical model of multi-vibrator resonators. Based on local resonance theory, we select the internal vibration method to design a 2D resonator comprising a copper outer frame and three copper internal vibrators connected by rubber bars. Some previous studies [14,17,20,21,35] have shown that the hollow square columns can produce a wider low-frequency bandgap, so a hollow square column is selected for the outer frame of the resonator in this study. Figure 3 shows the arrangement and dimensions of the resonator. Huang and Shi [23] pointed out that cylindrical barriers arranged in a hexagonal shape have a larger filling ratio compared to a square arrangement, which is more advantageous for a low-frequency wide bandgap. However, the literature [23] focuses on solid cylindrical barriers, which generate a bandgap by Bragg scattering, and the wide bandgap is a directional bandgap that attenuates elastic waves in one direction only. The resonator proposed in this paper generates bandgaps by the mechanism of local resonance and the bandgaps are omnidirectional bandgaps that can attenuate elastic waves in all directions. Therefore, the attenuation effect can be achieved by using an arrangement perpendicular to the building, as shown in Figure 3a. The square arrangement is chosen for simplicity of calculation, and the hexagonal arrangement of the resonator will be calculated in a subsequent study.

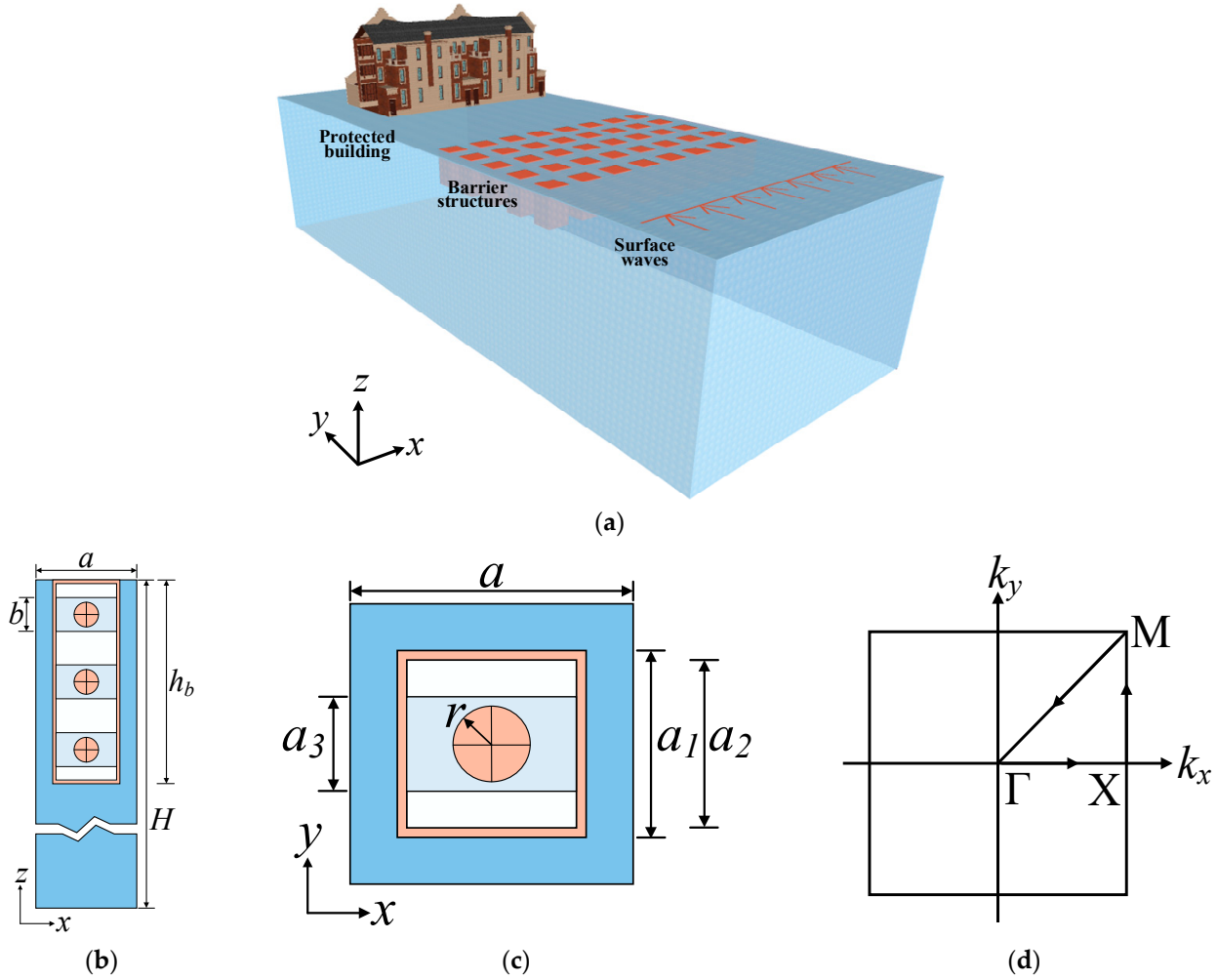


Figure 3. (**a**) Schematic diagram of the resonator; (**b**) lateral view of the unit cell; (**c**) internal view of the unit cell; (**d**) the first Brillouin zone.

The lattice constant is denoted by a, while a_1 and a_2 represent the outer and inner length of the square frame, respectively. h_b represents the depth of the resonator buried in the soil. The spacing between the three internal vibrators and the internal vibrator radius are represented by b and r. Simultaneously, the side length of the rubber connecting the internal vibrators to the outer frame is represented by a_3. The height of the unit cell is denoted by H. It has been demonstrated that when the height of the soil is greater than 10 times of the lattice constant, it has no significant effect on the bandgap created by the structure [55]. The dimensions and material parameters of the barrier are presented in Tables 2 and 3, respectively.

A surface waves resonator structure is created by arranging a unit cell periodically along the x–y direction. Firstly, the periodically arranged resonator can be simplified to a square unit cell based on phononic crystal and periodicity theory, and the first Brillouin zone is shown in Figure 3d. Then, the eigenfrequency of the unit cell can be calculated by scanned the path Γ-X-M-Γ in the first Brillouin zone in the eigenfrequency module of the finite element software COMSOL Multiphysics 5.6.

Table 2. Dimensional parameters of unit cell.

a (m)	a_1 (m)	a_2 (m)	a_3 (m)	r (m)	b (m)	h_b (m)	H (m)
1.5	1	0.9	0.5	0.2	1	3	20

Table 3. Material parameters of unit cell.

Material	Density (kg/m^3)	Young's Modulus (MPa)	Poisson's Ratio
Soil	1800	30	0.3
Rubber	1300	0.77	0.49
Copper	8950	8×10^4	0.3

The material is defined as linearly elastic and undamped, and soil properties are consistent with Biot's theory and are undamped. The governing equation used in the calculation of the eigenfrequencies can be written as

$$\rho(\mathbf{r})\ddot{\mathbf{u}}(\mathbf{r}) = \nabla[(\lambda(\mathbf{r}) + 2\mu(\mathbf{r}))(\nabla \cdot \mathbf{u}(\mathbf{r}))] - \nabla \times [\mu(\mathbf{r})\nabla \times \mathbf{u}(\mathbf{r})], \quad (6)$$

where $\mathbf{r} = (x, y, z)$ is the position vector, $\mathbf{u}$ is the displacement vector, ρ is the mass density, and λ and μ are the elastic constants. According to the Floquet–Bloch theorem, in the present periodic system, the solution of Equation (6), can be written as

$$\mathbf{u}(\mathbf{r}, t) = \exp(\mathrm{i}(\mathbf{k} \cdot \mathbf{r} - \omega t))\mathbf{u}_\mathbf{k}(\mathbf{r}). \quad (7)$$

where $\mathbf{u}_\mathbf{k}(\mathbf{r})$ is modulation function with the same periodicity as the elementary unit cell. The periodic boundary condition can be set around the unit cell and written as

$$\mathbf{u}(\mathbf{r} + \mathbf{a}, t) = \exp(\mathrm{i}(\mathbf{k} \cdot \mathbf{a}))\mathbf{u}(\mathbf{r}, t), \quad (8)$$

where $\mathbf{a}$ is the constant vector, which gives the repetition of a periodic structure. Combining the governing equation of Equation (6) and the periodic boundary condition of Equation (8), the dispersion relation of an infinite periodic system can be transferred into an eigenvalue problem of an elementary unit cell. The dispersion equation is an implicit function of wave vector $\mathbf{k}$ and angular frequency ω in mathematics,

$$\left(\mathbf{K} - \omega^2\mathbf{M}\right)\mathbf{U} = 0, \quad (9)$$

where $\mathbf{K}$ and $\mathbf{M}$ are the stiffness and mass matrices of the unit cell, respectively.

To eliminate the effect of structural dimensions, the relative bandgap can be used and written as

$$f_w = 2(f_u - f_l)/(f_u + f_l), \quad (10)$$

where f_u and f_l are the upper and lower bandgap frequencies, respectively.

4. Bandgaps of the Resonator

Rayleigh waves are a type of seismic surface waves, which carry most of the energy of the generated elastic waves within a frequency range of 0–20 Hz. The resonator designed focuses on attenuating Rayleigh waves within the frequency bandgap. To establish the unit cell model, the periodic boundary conditions are set around the unit cell to simulate the periodically arranged resonator. The fixed boundary conditions can be set at the bottom of the unit cell to simulate the soil in a semi-infinite space. Then, the eigenfrequency of the structure can be obtained by scanning the path Γ-X-M-Γ in the first Brillouin zone. However, the eigenfrequency diagram includes both body waves and surface waves. The previous research shows that the surface waves can be distinguished using the energy identification method [56]. The energy identification method and the model presented in the Pu et al. [56] was used to verify the accuracy of the finite element method. The model and the bandgaps are plotted in Figure 4a [56]. The periodic constant of the unit, the radius of pile, and the parameter about depth are taken as a = 0.8 m, r = 0.3 m, and h = 20a, respectively. The model comprises foam columns that are completely buried in the soil. The Young's modulus E, mass density ρ, and the Poisson ratio υ of foam and soil are taken as 37 MPa, 20 MPa, 60 kg/m^3, 1800 kg/m^3, 0.32, and 0.35, respectively. The

two materials are also assumed to be linearly elastic and undamped. The COMSOL is used for the eigenfrequencies calculation and the energy distribution parameter identification method is used for surface wave identification. It can be seen from Figure 4b that the present results are in agreement with the previous paper, which proves that the calculation method used in this study is correct.

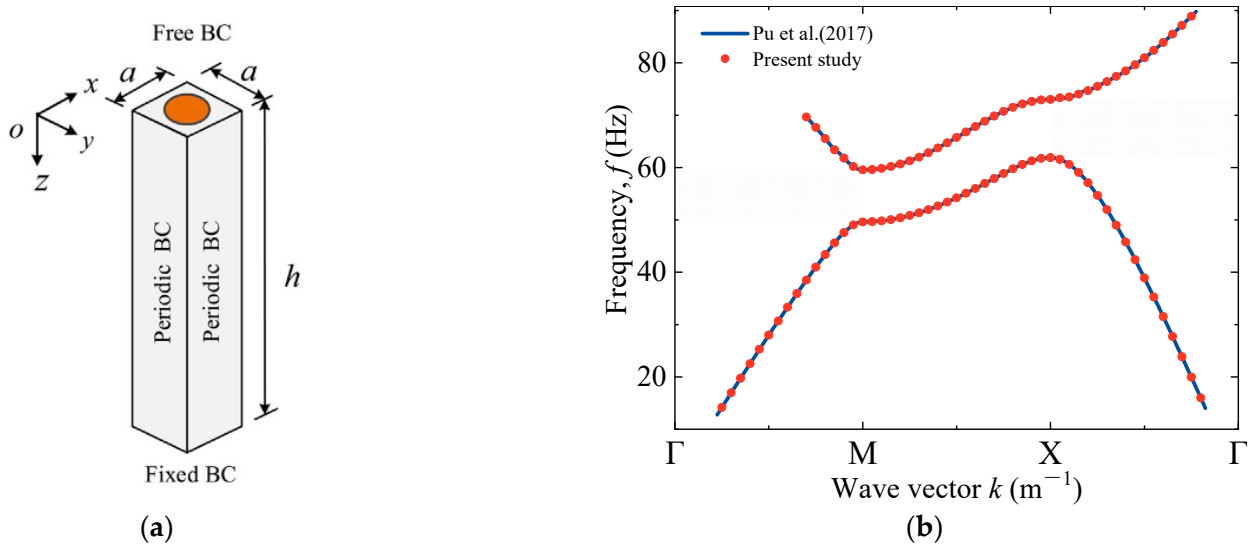


Figure 4. Verification for bandgaps in the previous paper: (**a**) the model; (**b**) the bandgaps (Pu et al. (2017) [56]).

Figure 5 shows the bandgaps for the multi-vibrator resonator. The first five bandgaps cover the frequency of the Rayleigh waves, and the ranges are 4.68–6.01 Hz, 6.03–9.31 Hz, 9.48–10.90 Hz, 10.94–18.72 Hz, and 18.79–22.01 Hz, respectively. All the bandgaps are omnidirectional and can attenuate Rayleigh waves in all directions.

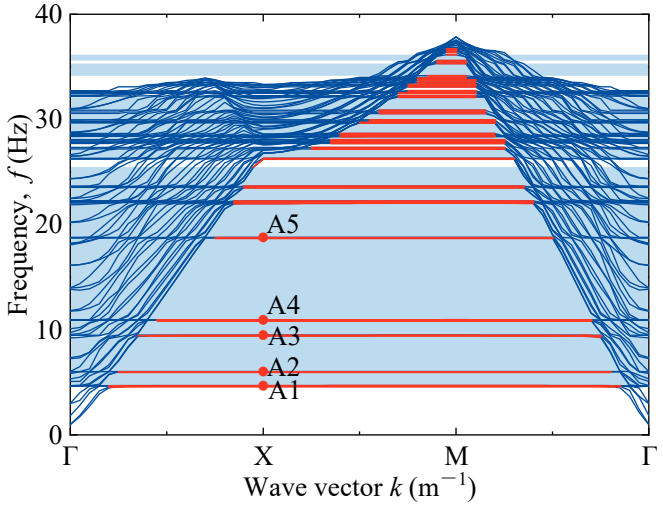


Figure 5. The bandgap of the resonator.

The finite element model is equivalent to the theoretical model and its dispersion curve is calculated to verify the accuracy of the finite element modeling. Given that the theoretical model is two-dimensional, the cross-section of the finite element model is taken as the two-dimensional equivalent section. The masses of the internal vibrators of the

resonator are the volume times the density, where the volume is the cross-sectional area times the unit length, as follows:

$$m_n = 1 \times \pi r^2 \rho_{copper}, n = 1, 2, 3, \tag{11}$$

The mass of the outer frame of the resonator is the volume times the density, where the volume is the cross-sectional area times the unit length, as follows:

$$m_0 = 1 \times (a_2 h_b - a_3(h_b - a_2 + a_3))\rho_{copper}, \tag{12}$$

The spring stiffnesses between the resonators and between the resonator and its internal vibrators are provided by that of the soil and rubber, respectively. The stiffness formula is as follows:

$$k_n = \frac{E_n A_n}{L_n}, n = 0,\ 1,\ 2,\ 3, \tag{13}$$

where E_n is the Young's modulus of soil or rubber. A_n is the area of the resonator in contact with the soil or rubber in the plane normal to the direction of spring action. L_n is the length of soil or rubber equivalent to the spring. The equivalent parameters are shown in Table 4. The equivalent model dispersion curves can be obtained by Table 4 and Equation (4), as shown in Figure 6. The bandgap of the equivalent model is from 4.36 Hz to 5.99 Hz in Figure 6, while the first bandgap of the finite element model is from 4.68 Hz to 6.01 Hz. The errors in the upper and lower boundaries are minimal, amounting to 0.3% and 6.8%, respectively. The reason for the errors may be the different dimensions of the finite element model and the theoretical model. In the finite element model, the vibration displacements of the resonator may be distributed in the x, y, and z directions, while that of the resonator can only be generated along the axis of the spring. Nevertheless, the two-dimensional theoretical resonator model proposed in this study can effectively analyze the lower boundary of the bandgap.

Table 4. Equivalent parameters of the resonator.

m_0 (kg)	m_1 (kg)	m_2 (kg)	m_3 (kg)	k_0 (N/m)	k_1 (N/m)	k_2 (N/m)	k_3 (N/m)
3490.50	1124.69	1124.69	1124.69	540,000,000.00	427,777.78	427,777.78	427,777.78

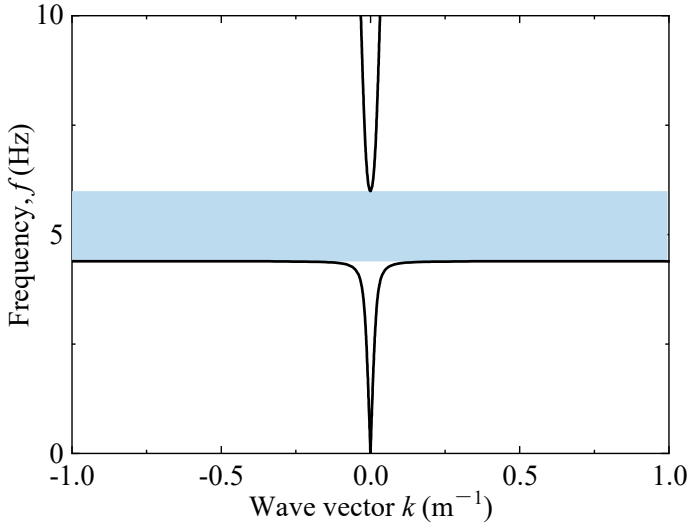


Figure 6. The dispersion curve of the equivalent model.

The special points are selected at the upper and lower boundary of bandgaps to investigate the mechanism of the bandgap generated by the resonators. Figure 5 shows

the points of the resonator for A1, A2, A3, A4, and A5, respectively. Additionally, Figure 7 displays the vibration modal diagrams. As illustrated in Figure 7, the vibrations of surface waves modes are primarily concentrated in the internal vibrators of the resonator. In Figure 7a, the vibrational displacements generated by the elastic waves are concentrated in the second and third vibrators, and the second vibrator triggers the greatest displacement. Furthermore, the second vibrator produces a horizontal displacement along the y-axis, while the third vibrator produces a horizontal displacement in the opposite direction. As illustrated in Figure 7b, the vibrational displacement occurs primarily in the first vibrator, which rotates clockwise along the y–z plane. The maximum displacement is observed on the four edges of the rubber bar. In Figure 7c, the horizontal vibrational displacement is concentrated in the second vibrator along the x-axis, which causes stretching on one side of the rubber bar and compression on the other side. Small displacements are observed in the third vibrator, which are in the opposite direction to the second vibrator. The maximum displacement occurs on the copper ball and on the compressed side of the rubber bar. Figure 7d illustrates that a rotation is produced in three dimensions in the first and second vibrators. In addition to horizontal displacements in the x- and y-axis directions, rotations in the y–z plane were also observed. The maximum displacement occurs on the edge of the rubber bar. As illustrated in Figure 7e, the third vibrator produced two rotational displacements in opposite directions in the y–z plane. The maximum displacement occurs on the four edges of the rubber bar. The energy in the elastic waves is consumed by the vibrations that are generated by the internal vibrators, which can attenuate the elastic waves and protect the building situated behind the resonator.

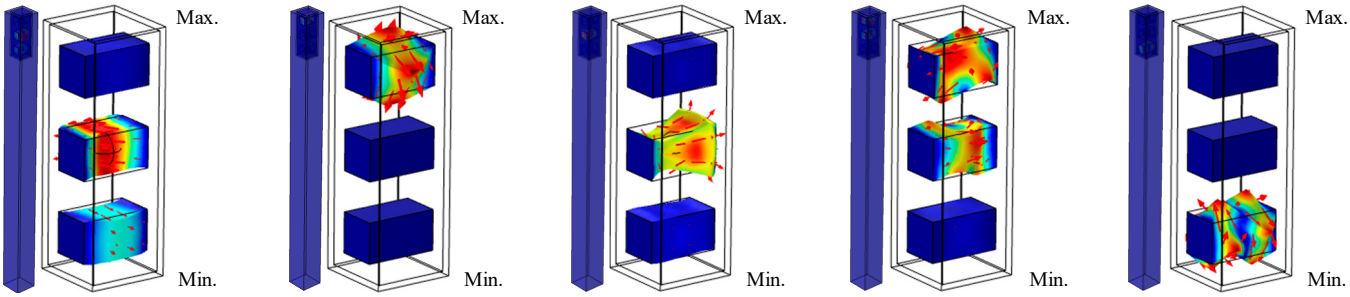


Figure 7. The vibration modes of (**a**) A1; (**b**) A2; (**c**) A3; (**d**) A4; (**e**) A5.

5. Transmission Spectrum Analysis

In Section 4, the bandgaps of the resonator are calculated at infinite periods. However, it is not possible to set up an infinite period resonator in practical engineering. Therefore, this section will calculate the transmission spectrum to verify the attenuation effect of the proposed resonator on elastic waves.

The transmission spectrum function is defined as

$$\mathrm{FRF} = 20 \times \log_{10}(u_2/u_1), \tag{14}$$

where u_1 and u_2 are the displacements at the pickup positions without and with barrier, respectively.

Figure 8 shows the finite element model of the resonator periodically arranged in soil. To simulate the attenuation effect of the resonator on elastic waves in a semi-infinite space, a perfectly matched layer (PML) is set at the boundary of the model to absorb the elastic waves, which can reduce the reflection of elastic waves and improve the accuracy of the results. A distance of $16a$ is set between the excitation and the resonator to convert the unit line load into surface waves. To determine the attenuation of elastic waves by the soil, the transmission spectrum analysis with no barrier can be calculated. A unit line load is applied along the negative direction of the z-axis at the excitation position and the

displacement is collected at the pickup position. Then, the transmission spectrum diagram is calculated using Equation (14).

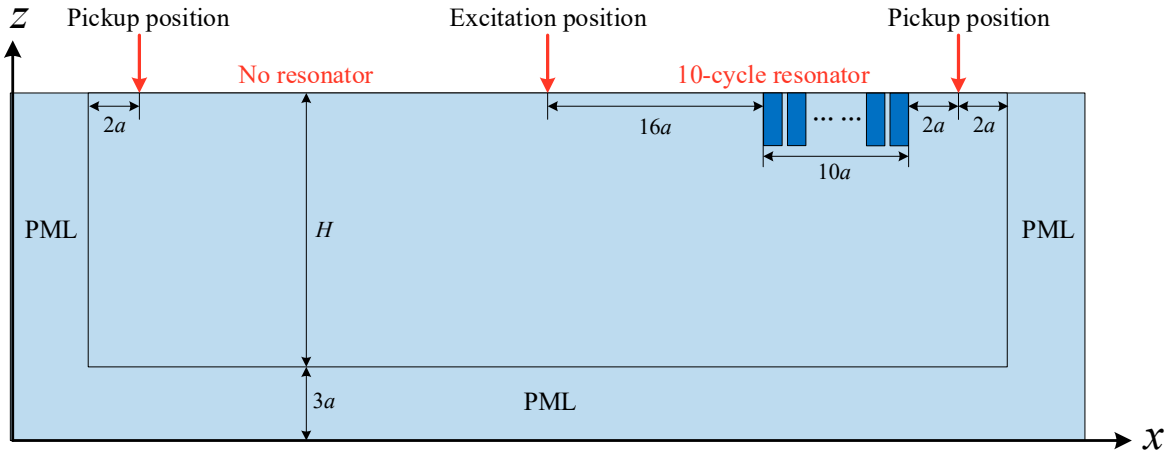


Figure 8. The transmission spectrum analysis model with the resonator.

Figure 9 shows the transmission spectrum diagram of the 10-cycle resonator within the frequency of the Rayleigh surface waves. It can be seen that the resonator effectively attenuates the elastic waves in the bandgap. The maximum attenuation values reached −19.85 dB and −21.67 dB at 5.14 Hz in the first bandgap, and 10.66 Hz in the third bandgap, respectively.

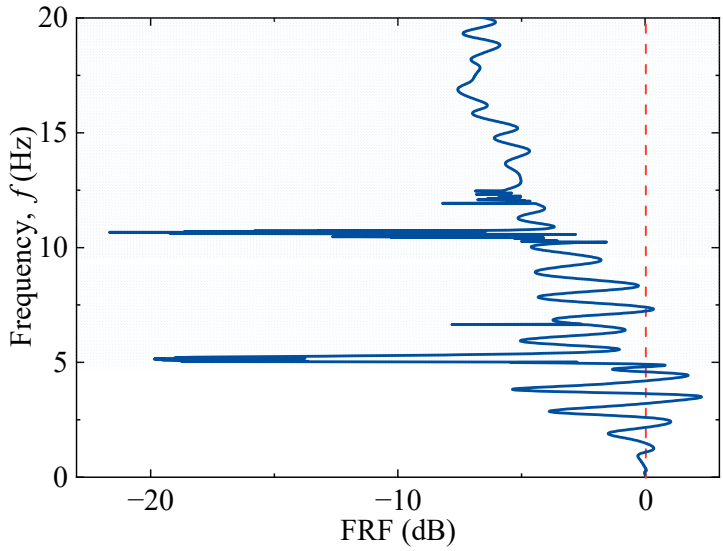


Figure 9. The transmission spectrum diagram.

To further investigate the mechanism of attenuation of elastic waves by the resonator, the total displacements at 1 Hz and 5.1 Hz were analyzed and are compared in Figure 10. As shown in Figure 10a,b, it can be seen that the resonator cannot attenuate elastic waves with the frequency of 1 Hz, which means that the propagation path of the elastic waves remains unaltered and the energy carried in the elastic waves is not reduced.

In Figure 10c,d, the elastic waves for 5.1 Hz are greatly attenuated by the resonator. As shown in Figure 10c, the elastic waves emitting from the excitation point are gradually converted into body and surface waves. In Figure 10d, the resonator blocks the surface waves and changes the surface waves into body waves transmitting to the deep soil, resulting in minimal vibration of the soil surface behind the resonator. The vibrations of soil in front of the resonator generated by the elastic waves are intensified. Some of the energy

of the elastic waves is converted into body waves, while the remainder is concentrated in the internal vibrators of the resonator. Figure 10e illustrates the vibration of the internal vibrators of the resonator when the excitation frequency of the surface waves is 5.1 Hz. It can be found that the internal vibrators produce a substantial vibration, which consumes the energy of the elastic waves.

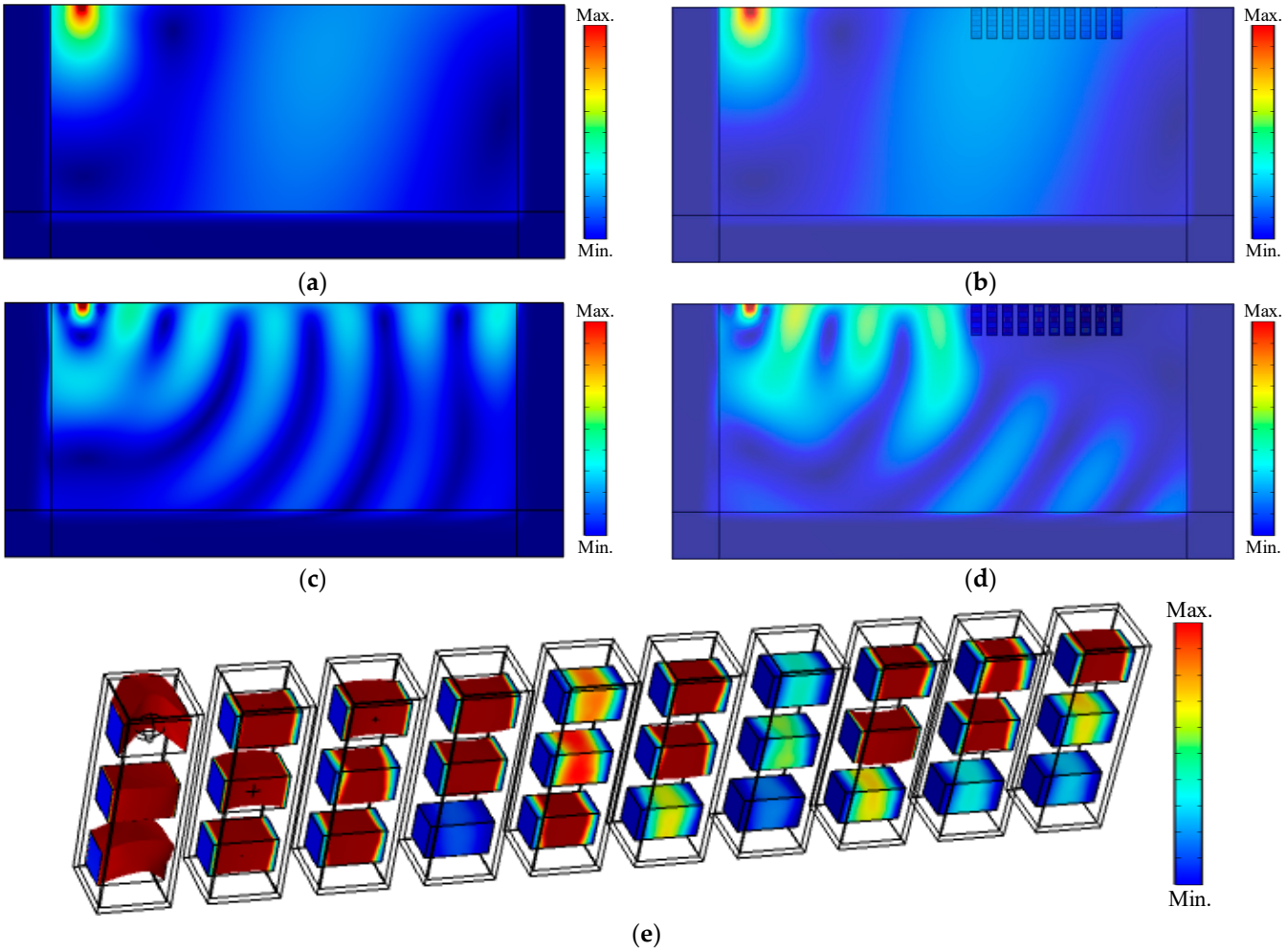


Figure 10. Displacement diagram at (**a**) 1 Hz without resonator; (**b**) 1 Hz with 10-cycle resonator; (**c**) 5.1 Hz without resonator; (**d**) 5.1 Hz with 10-cycle resonator; (**e**) 5.1 Hz with internal structures.

6. Time History Analysis

Time history analysis of artificial and seismic waves is used to further verify the attenuation of the resonator in this section. The Hanning modulation window function is selected for the artificial waves, and is shown as follows:

$$A_{in} = \left\{ \begin{array}{l} \frac{1}{A_{\max}}\left[1-\cos\left(\frac{2\pi f_c t}{C}\right)\right] \times \sin(2\pi f_c t), 0 \le t \le \frac{C}{f_c} \\ 0, t \ge \frac{C}{f_c} \end{array} \right\}, \quad (15)$$

where A_{max} is the maximum amplitude of the artificial waves, f_c is the center frequency, C is the periodic number, and t is the duration.

Figure 11 shows the numerical model of the resonator arranged periodically along the x direction. To simulate the semi-infinite space, a low-reflection boundary condition is set around the model, which is used to reduce the reflection of elastic waves at the boundary. The displacement of the artificial waves or seismic waves will be applied at the excitation position, and the acceleration amplitude will be collected at the pickup position. The center

frequency of the artificial waves is selected as 5.1 Hz in the bandgap range and 1 Hz out of the frequency bandgap, respectively, as shown in Figure 12. The acceleration time history of the El Centro waves is shown in Figure 13.

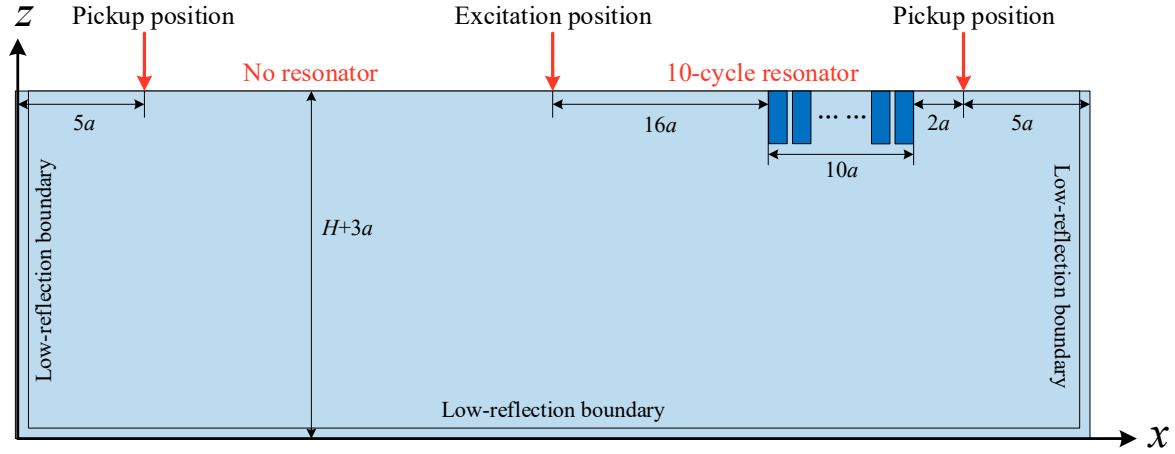


Figure 11. The time history analysis model with the resonator.

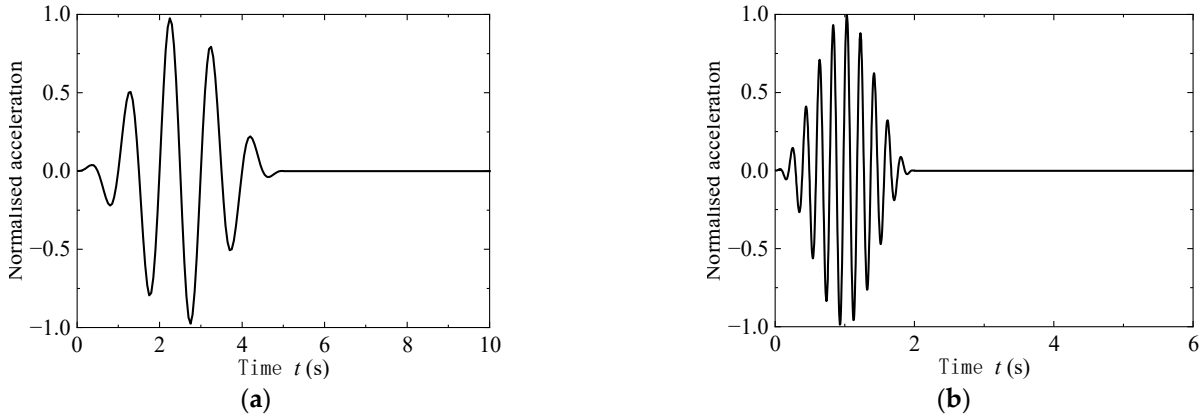


Figure 12. The acceleration of artificial waves with a center frequency of (**a**) 1 Hz; (**b**) 5.1 Hz.

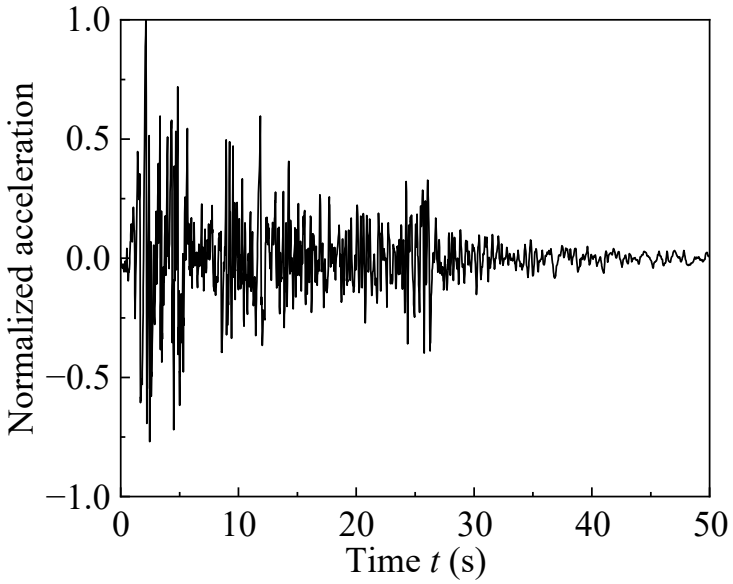


Figure 13. The acceleration of El Centro.

Figure 14 shows the acceleration response of the resonator under artificial waves with main frequencies of 1 Hz and 5.1 Hz. It can be seen that the resonator can effectively attenuate the artificial waves when the excitation frequency of 5.1 Hz falls into the frequency bandgap, which means that the acceleration of the artificial waves with the frequency of 5.1 Hz can be reduced by 65%, as shown in Figure 14b, whereas the resonator almost cannot mitigate the artificial waves when the central frequency of 1 Hz falls outside the frequency bandgap, as shown in Figure 14a.

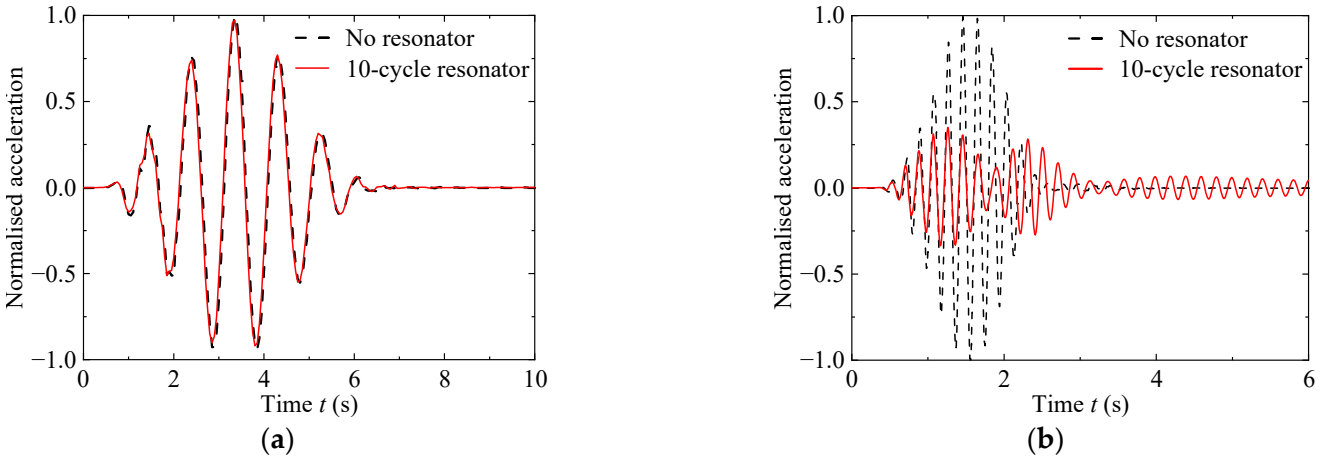


Figure 14. Acceleration response of the resonator under artificial waves (**a**) at 1 Hz; (**b**) at 5.1 Hz.

Figure 15 illustrates the acceleration time history and the response spectrum of the resonator under the El Centro seismic wave. Figure 15a demonstrates that the resonator significantly attenuates the El Centro seismic wave during the time period of 0–50 s. The resonator reduces the peak of the seismic waves to 0.39 with an attenuation rate of 61%. In Figure 15b, the resonator significantly attenuates the amplitude of the El Centro seismic wave in the bandgap with an attenuation rate of 65.75%. These results demonstrate that the resonator can effectively attenuate seismic waves within the frequency bandgap of the resonators.

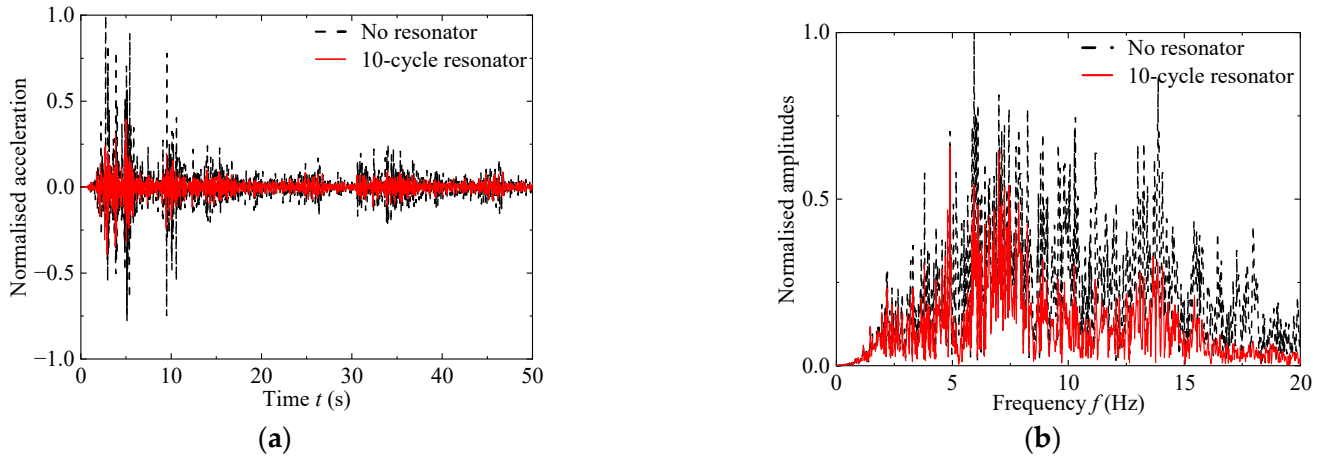


Figure 15. Acceleration response of the resonator under El Centro: (**a**) acceleration time history and (**b**) the response spectrum of El Centro.

In Figure 15a, the maximum acceleration of the El Centro seismic wave occurs at 2.75 s with the resonator, while it is only 0.00958 at 2.75 s with the 10-cycle resonator. In order to further analyze the attenuation of the El Centro seismic wave by the 10-cycle resonator, the total displacements of the seismic waves with and without the resonator are shown in Figure 16 at 2.75 s. As shown in Figure 16a, the surface of the soil body at the pickup point

produced a large ground displacement without the barrier. The upper parts of the soil body produced many concentrated displacements, with the largest concentrated displacement occurring in the upper part of the soil body at the pickup point. In Figure 16b, it can be seen that the surface displacement of the soil body behind the resonator is significantly attenuated and the displacement of the soil body below the resonator is also attenuated. Therefore, it further indicates that the resonator not only effectively attenuates the surface waves of seismic waves, but also converts part of the seismic waves into body waves and also proves the conclusions drawn from the previous section.

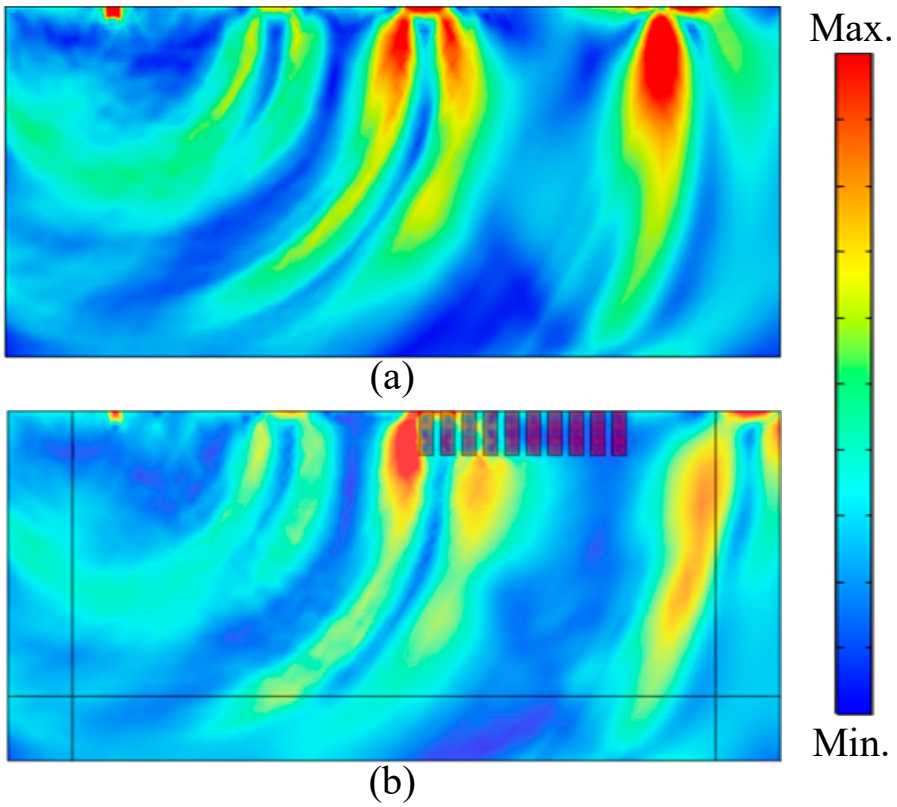


Figure 16. Displacement diagram at (**a**) 2.75 s without resonator; (**b**) 2.75 s with 10-cycle resonator.

7. Effect of Resonator Size

The size of the resonator is the key factor affecting the bandgaps. Based on the mechanism of bandgap generation in resonators as well as the previous research results [7,10,21,23,35–37,48], this study analyzes the effects of the outer frame size and the radius of the internal vibrator of the resonator on the bandgap, respectively. The outer frame size of the resonator is related to the other dimensions of the resonator structure. In order to ensure that the other important parameters of the structure remain unchanged (the size of the internal vibrator and the thickness of the frame), the length of the rubber is increased while increasing the size of the outer frame, and the other parameters of the resonator are shown in Table 2. The bandgap is calculated in the range of 0–20 Hz for frame sizes a_1 of 1.0 m, 1.1 m, 1.2 m, and 1.3 m. Frequency dispersion curves are shown in Figure 17. In calculating the effect of the radius of the internal vibrator on the bandgap range, other parameters are kept constant, as shown in Table 2, and the bandgap is calculated in the range of 0–20 Hz when the radius r of the internal vibrator is 0.05 m, 0.10 m, 0.15 m, and 0.20 m, respectively, and frequency dispersion curves are shown in Figure 18.

In Figure 17, it can be seen that when the outer frame size a_1 is 1 m, the first five bandgaps can cover the frequency range of the Rayleigh wave. As the frame size a_1 increases, the number of bandgap increases to cover the frequency range of the Rayleigh wave, and the number of bandgaps are 6, 7, and 8 when a_1 is 1.1 m, 1.2 m, and 1.3 m, respectively. As the outer frame size a_1 increases from 1 m to 1.3 m, the upper and lower

boundaries of the first five bandgaps are decreasing, and the lower boundary of the first bandgap is 3.4249 Hz when a_1 is 1.3 m, which is 1.2546 Hz lower compared to 4.6795 Hz when a_1 is 1 m; the widths of the first, second, fourth, and fifth bandgaps are decreasing, while the third bandgap has a slight increase in width. The larger the outer frame size a_1, the more the lower boundary of the bandgap decreases. When increasing the outer frame size, the length of the rubber connecting the internal vibrator to the outer frame increases accordingly, and the increase in rubber length helps to increase the vibration displacement of the internal vibrator as well as consume the energy of the elastic wave. Therefore, as the size of the outer frame of the resonator and the length of the rubber increase, the lower boundary of the bandgap generated by the resonator gradually decreases, which contributes to the attenuation of the low-frequency elastic waves and enables the generation of more bandgaps.

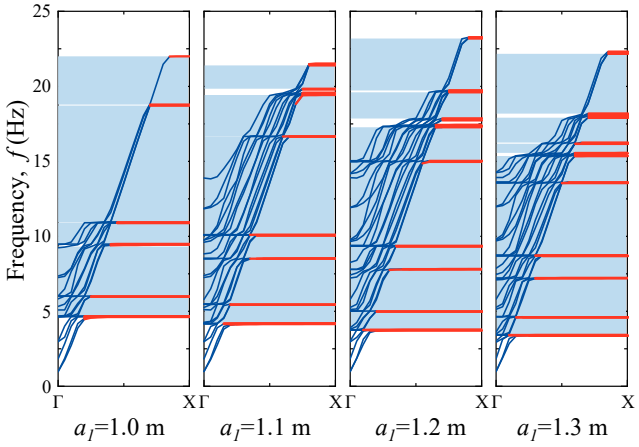


Figure 17. Frequency dispersion curves for different outer frame sizes.

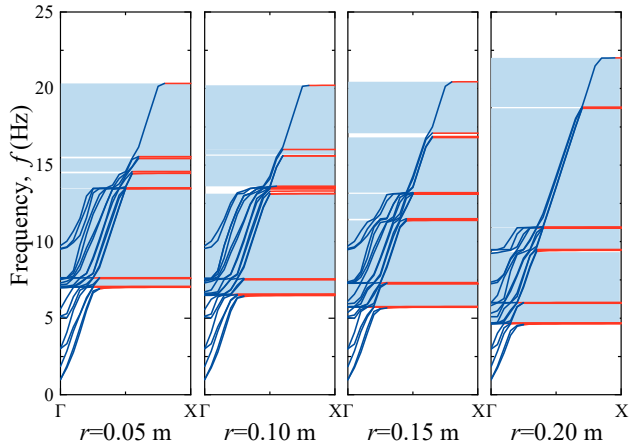


Figure 18. Frequency dispersion curves for different vibrator sizes.

In Figure 18, it can be concluded that the lower boundary of the bandgap decreases as the radius of the internal vibrators increase. The lower boundary of the bandgap is 7.0796 Hz when the radius of the internal vibrators r = 0.05 m and decreases to 4.6795 Hz when the radius of the internal vibrators r = 0.20 m. From the previous analysis of the vibration diagrams of the resonator, it can be seen that the bandgap of the resonator is produced due to the absorption of the energy of the elastic wave by the internal vibrators. The larger the radius of the vibrators, the more elastic wave energy is absorbed by the internal vibrators, so the lower the bandgap that can be generated.

Based on the analysis of the parameters of the resonator, it is clear that the larger the resonator, the lower the frequency bandgap, and the larger the radius of the internal vibrators, the lower the frequency bandgap.

8. Effect of Damping

As mentioned above, soil properties are consistent with Biot' s theory and undamped in the previous sections. While the actual soil has damping characteristics, the influence of the soil damping is considered in this section. The Rayleigh damping is used in this study, and the equation for Rayleigh damping is written as follows:

$$\boldsymbol{C} = \alpha_{dM}\boldsymbol{M} + \beta_{dK}\boldsymbol{K}, \tag{16}$$

where α_{dM} is mass damping coefficient, and β_{dK} is stiffness damping coefficient. Rayleigh damping is affected by the frequency range and damping ratio of the structure. In this section, the frequency range of the structure is set as 0.1–20 Hz and can be written as

$$\begin{cases} f_1 = 0.1 \text{ Hz} \\ f_2 = 20 \text{ Hz}, \end{cases} \tag{17}$$

where f_1 and f_2 are the lower and upper boundaries of the structural frequency, respectively. The angular frequencies can be calculated as follows:

$$\begin{cases} \omega_1 = 2\pi f_1 = 0.628 \\ \omega_2 = 2\pi f_2 = 125.664, \end{cases} \tag{18}$$

where ω_1 and ω_2 are the lower and upper boundaries of the angular frequency for structure, respectively. Rayleigh damping coefficients are written as

$$\begin{cases} \frac{\alpha_{dM}}{2\omega_1} + \frac{\beta_{dK}\omega_1}{2} = \xi \\ \frac{\alpha_{dM}}{2\omega_2} + \frac{\beta_{dK}\omega_2}{2} = \xi, \end{cases} \tag{19}$$

where ξ is damping ratio.

The soil damping ratio is from 0.01 to 0.08, with a general value of 0.05 taken in this study. The mass and stiffness damping coefficients of Rayleigh damping are calculated to be 0.0625 s^{-1} and 0.0008 s, respectively. The time history analysis of the El Centro seismic wave with soil damping is calculated and the results are shown in Figure 19. It can be found in Figure 19a that the soil damping significantly attenuates the El Centro seismic wave with a maximum acceleration of 0.2286, and the attenuation efficiency of the resonator considering soil damping is improved by 32.67% compared to the case of the resonator without soil damping. Figure 19b illustrates that soil damping attenuates frequencies within 1.96–20 Hz, with a maximum amplitude of 0.477. However, soil damping does not attenuate frequencies from 0 Hz to 1.96 Hz.

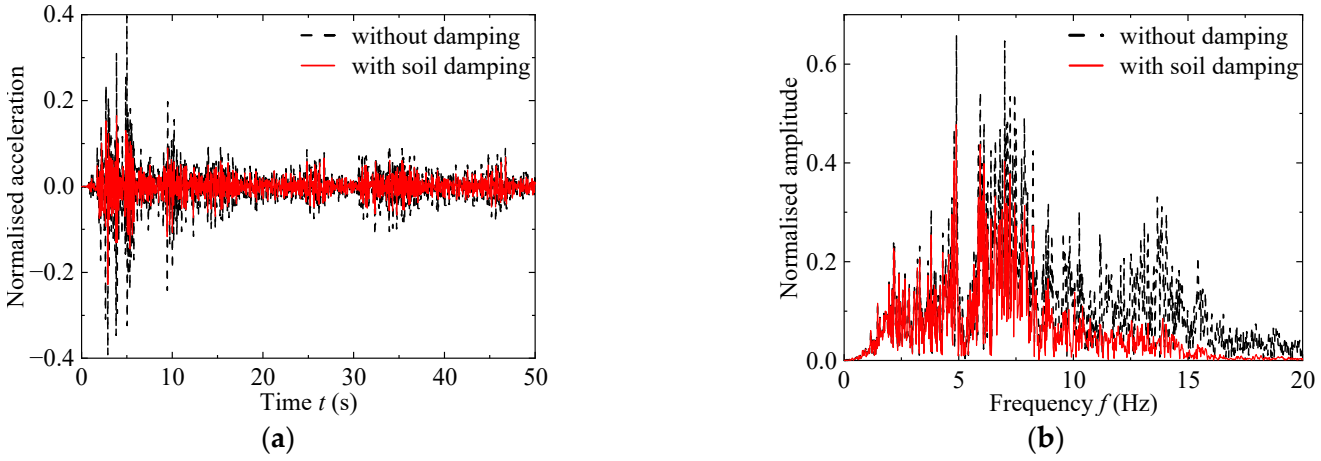


Figure 19. (**a**) Acceleration time history of El Centro; (**b**) the response spectrum of El Centro with soil damping.

Simultaneously, the material damping of the rubber and copper is also considered. Figure 20 shows the acceleration responses of the resonator considering the soil and material damping. It can be found that the attenuation by the resonator considering both soil and material damping is almost the same as when only considering soil damping, which indicates that material damping has a negligible effect on the attenuation performance of the resonator.

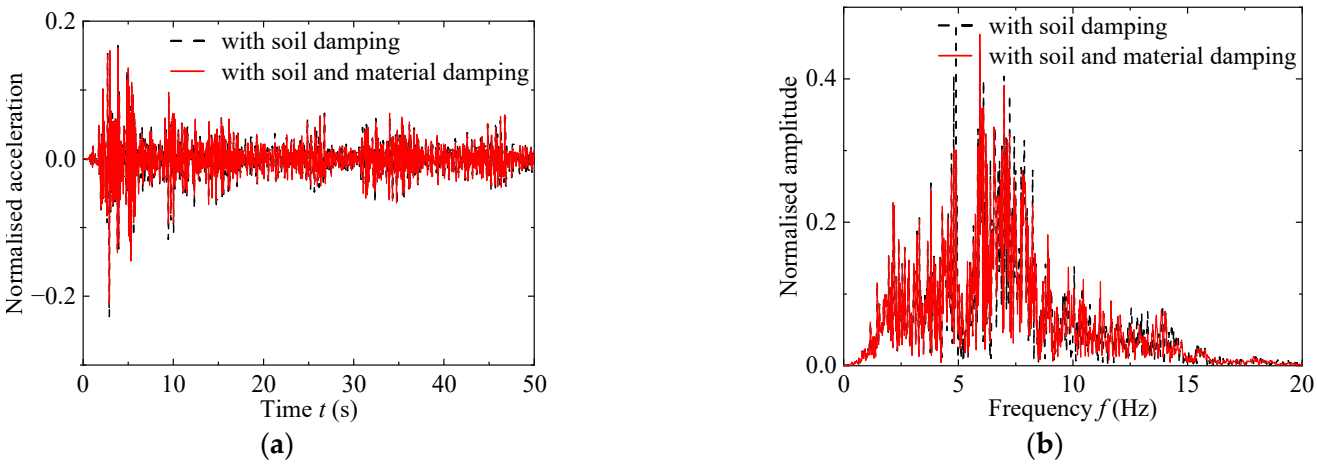


Figure 20. (**a**) Acceleration time history of El Centro; (**b**) the response spectrum of El Centro with soil and material damping.

9. Conclusions

In this study, a low-frequency bandgap resonator with three internal vibrators was investigated using theoretical and finite element methods, respectively. Firstly, a resonator with three internal vibrators was proposed based on the mass spring theory. Secondly, the attention effect of the resonator was studied through transmission spectrum and time history analysis. Finally, the effects of soil and material damping of the resonator on the mitigation of the Raleigh waves were discussed and compared. The main conclusions were obtained as follows.

(1) A theoretical model of the resonator was proposed based on the local resonance theory, and the mass-spring theory was used to establish the dynamic equilibrium equation. The results showed that the resonator can generate a wide low-frequency bandgap.

(2) The resonator has omnidirectional bandgaps with a first five bandgaps (4.68–22.01 Hz) covering the frequency of Rayleigh surface waves. It was indicated that the mechanism of bandgap of the resonator is a local resonance phenomenon through vibration modal analysis.

(3) It was demonstrated from transmission spectrum of the 10-cycle resonator that the resonator can effectively attenuate elastic waves within the bandgap. The reason is that the resonator converts surface waves into body waves and the internal vibrators consume the energy of elastic waves.

(4) The time history analysis results show that the resonator can decrease the accelerations of artificial waves or seismic waves by 61% when the main frequency is in the bandgap of the resonator. The amplitude of the El Centro seismic wave in the bandgap was attenuated by 65.75%.

(5) The effects of soil and material damping of the resonator on the attenuation of seismic waves were, respectively, considered and calculated. The results showed that the attenuation rate of the acceleration was 32.67% when the numerical model considered the soil damping, while the material damping of the resonator had little effect in attenuating seismic waves.

(6) In this study, the resonators could attenuate seismic surface waves in the main frequency range of 4.68 Hz to 22.01 Hz and it was found that a 10-cycle resonator could effectively attenuate El Centro seismic waves. Moreover, the higher the number of resonators, the better the attenuation effect. Therefore, the number of resonators can be flexibly

arranged according to the earthquake magnitude, building strength, and site conditions in practical engineering applications.

(7) In this study, a resonator with some bandgaps from 4.68 Hz to 22.01 Hz was proposed, but the study is not perfect and there are still many deficiencies, which will be further improved. Firstly, a structure that is not only small in size but also has a lower frequency bandgap to attenuate seismic waves with ultra-low frequency as the main frequency can be developed. Then, scaled or full-scale tests can be conducted to further demonstrate the actual attenuation of elastic waves by the resonator structure. Finally, specific protected building structures will be added to the finite element model calculations to analyze the vibration displacements of the building with and without resonator protection and to further analyze the protective effect of the resonator on the building.

(8) The computational method of machine learning can be applied to the calculation of seismic surface wave attenuation by resonators, such as analyzing the dispersion curves of the resonators, estimating the amplitude of vibrations generated by the resonators and the ground under different conditions, optimizing the parameter design of the resonators, and calculating the theoretical analysis of the resonators in terms of elastic dynamics. These machine learning aspects will be studied and analyzed later.

Author Contributions: Conceptualization, C.Z. and H.J.; methodology, C.Z. and H.J.; software, H.J.; validation, C.Z., Y.C. and J.L.; formal analysis, C.Z.; investigation, H.J.; resources, C.Z.; data curation, H.J.; writing—original draft preparation, H.J.; writing—review and editing, C.Z.; visualization, Y.C.; supervision, J.L.; project administration, Y.C.; funding acquisition, C.Z. All authors have read and agreed to the published version of the manuscript.

Funding: This work is supported by Xinjiang Natural Science Key Fund under Grant No. 2022D01D33 and the National Natural Science Foundation of China Upper-level Project under Grant No. 52278302.

Data Availability Statement: Data are contained within the article.

Conflicts of Interest: The authors declare no conflicts of interest.

References

1. Nicoletti, V.; Arezzo, D.; Carbonari, S.; Grar, F. Detection of infill wall damage due to earthquakes from vibration data. *Earthq. Eng. Struct. Dyn.* **2023**, *52*, 460–481. [CrossRef]
2. Benchabane, S.; Khelif, A.; Rauch, J.Y.; Robert, L.; Laude, V. Evidence for complete surface wave band gap in a piezoelectric phononic crystal. *Phys. Rev. E* **2006**, *73*, 065601. [CrossRef] [PubMed]
3. Fu, Z.J.; Li, L.; Gu, Y. A localized meshless collocation method based on semi-analytical basis functions for bandgap calculation of elastic waves in phononic crystals. *Proc. Appl. Math. Mech.* **2020**, *20*, e202000021. [CrossRef]
4. Kushwaha, M.S.; Halevi, P.; Dobrzynski, L.; Rouhani, B.D. Acoustic band structure of periodic elastic composites. *Phys. Rev. Lett.* **1993**, *71*, 2022. [CrossRef] [PubMed]
5. Laude, V.; Wilm, M.; Benchabane, S.; Khelif, A. Full band gap for surface acoustic waves in a piezoelectric phononic crystal. *Phys. Rev. E* **2005**, *71*, 036607. [CrossRef]
6. Trzaskowska, A.; Hakonen, P.; Wiesner, M.; Mielcarek, S. Generation of a mode in phononic crystal based on 1D/2D structures. *Ultrasonics* **2020**, *106*, 106146. [CrossRef]
7. Luo, Y.M.; Huang, T.T.; Zhang, Y.; Xu, H.H.; Xie, Y.M.; Ren, X. Novel meter-scale seismic metamaterial with low-frequency wide bandgap for Lamb waves. *Eng. Struct.* **2023**, *275*, 115321. [CrossRef]
8. Guo, J.J.; Cao, J.Z.; Xiao, Y.; Shen, H.J.; Wen, J.H. Interplay of local resonances and Bragg band gaps in acoustic waveguides with periodic detuned resonators. *Phys. Lett. A* **2020**, *12*, 55. [CrossRef]
9. Khelif, A.; Achaoui, Y.; Benchabane, S.; Laude, V.; Aoubiza, B. Locally resonant surface acoustic wave band gaps in a two-dimensional phononic crystal of pillars on a surface. *Phys. Rev. B* **2010**, *81*, 214303. [CrossRef]
10. Muhammad; Lim, C.W. Elastic waves propagation in thin plate metamaterials and evidence of low frequency pseudo and local resonance bandgaps. *Phys. Lett. A* **2019**, *383*, 2789–2796. [CrossRef]
11. Muhammad; Lim, C.W.; Reddy, J.N. Built-up structural steel sections as seismic metamaterials for surface wave attenuation with low frequency wide bandgap in layered soil medium. *Eng. Struct.* **2019**, *188*, 440–451. [CrossRef]
12. Zeng, C.; Zhao, C.; Zeighami, F. Seismic surface wave attenuation by resonant metasurfaces on stratified soil. *Earthq. Eng. Struct. D* **2022**, *51*, 1201–1223. [CrossRef]
13. Zhao, X.M.; Liu, X.N.; Hu, G.K. Elastic metamaterials with local resonances: An overview. *Theor. Appl. Mech. Lett.* **2012**, *2*, 041001. [CrossRef]

14. Miniaci, M.; Krushynska, A.; Bosia, F.; Pugno, N.M. Large scale mechanical metamaterials as seismic shields. *New J. Phys.* **2016**, *18*, 083041. [CrossRef]
15. Witarto, W.; Wang, S.J.; Yang, C.Y.; Wang, J.J.; Mo, Y.L.; Chang, K.C.; Tang, Y. Three-dimensional periodic materials as seismic base isolator for nuclear infrastructure. *AIP Adv.* **2019**, *9*, 045014. [CrossRef]
16. Liu, Z.; Chan, C.T.; Sheng, P. Analytic model of phononic crystals with local resonances. *Phys. Rev. B* **2005**, *71*, 014103. [CrossRef]
17. Wang, Y.; Yang, F.; Yang, J.S.; Tong, L.L.; Li, S.; Liu, Q.; Hou, G.L.; Sun, P.D.; Xing, M.; Zheng, G. Study on vibration damping performance of a petal-shaped seismic metamaterial. *Structures* **2023**, *56*, 104898. [CrossRef]
18. Achaoui, Y.; Antonakakis, T.; Brûlé, S.; Craster, R.V.; Enoch, S.; Guenneau, S. Clamped seismic metamaterials: Ultra-low frequency stop bands. *New J. Phys.* **2017**, *19*, 063022. [CrossRef]
19. Achaoui, Y.; Ungureanu, B.; Enoch, S.; Brule, S.; Guenneau, S. Seismic waves damping with arrays of inertial resonators. *Extrem. Mech. Lett.* **2016**, *8*, 30–37. [CrossRef]
20. Cheng, Z.; Shi, Z. Vibration attenuation properties of periodic rubber concrete panels. *Constr. Build. Mater.* **2014**, *50*, 257–265. [CrossRef]
21. Du, Q.; Zeng, Y.; Huang, G.; Yang, H.W. Elastic metamaterial-based seismic shield for both Lamb and surface waves. *AIP Adv.* **2017**, *7*, 075015. [CrossRef]
22. Hajjaj, M.M.; Tu, J.W. A seismic metamaterial concept with very short resonators using depleted uranium. *Arch. Appl. Mech.* **2021**, *91*, 2279–2300. [CrossRef]
23. Huang, J.; Shi, Z. Application of Periodic Theory to Rows of Piles for Horizontal Vibration Attenuation. *Int. J. Geomech.* **2013**, *13*, 132–142. [CrossRef]
24. Liu, Z.; Zhang, X.; Mao, Y.; Zhu, Y.Y.; Yang, Z.Y.; Chan, C.T.; Sheng, P. Locally Resonant Sonic Materials. *Science* **2000**, *289*, 1734–1736. [CrossRef]
25. Mei, J.; Liu, Z.; Shi, J.; Tian, D.C. Theory for elastic wave scattering by a two-dimensional periodical array of cylinders: An ideal approach for band-structure calculations. *Phys. Rev. B* **2003**, *67*, 245107. [CrossRef]
26. Pu, X.B.; Shi, Z.F.; Xiang, H.J. Feasibility of ambient vibration screening by periodic geofoam-filled trenches. *Soil Dyn. Earthq. Eng.* **2018**, *104*, 228–235. [CrossRef]
27. Pu, X.B.; Shi, Z.F. Surface-wave attenuation by periodic pile barriers in layered soils. *Constr. Build. Mater.* **2018**, *180*, 177–187. [CrossRef]
28. Zeng, Y.; Xu, Y.; Yang, H.W.; Muzamil, M.; Xu, R.; Deng, K.K.; Peng, P.; Du, Q.J. A Matryoshka-like seismic metamaterial with wide band-gap characteristics. *Int. J. Solids Struct.* **2020**, *185–186*, 334–341. [CrossRef]
29. Zhao, C.F.; Gao, Z.W.; Zhang, X. Low-Frequency Surface Wave Attenuation of Multi Point Mass Resonance Metamaterials. *J. Vib. Eng. Technol.* **2024**. [CrossRef]
30. Liu, Y.; Yang, J.; Yi, X.; Guo, W.J.; Feng, Q.S.; Chronopoulos, D. Enhanced vibration suppression using diatomic acoustic metamaterial with negative stiffness mechanism. *Eng. Struct.* **2022**, *271*, 114939. [CrossRef]
31. Colombi, A.; Colquitt, D.; Roux, P.; Guenneau, S.; Craster, R.V. A seismic metamaterial: The resonant metawedge. *Sci. Rep.* **2016**, *6*, 27717. [CrossRef]
32. Cheng, Z.; Shi, Z. Novel composite periodic structures with attenuation zones. *Eng. Struct.* **2013**, *56*, 1271–1282. [CrossRef]
33. Chen, Z.; Wang, G.; Lim, C.W. Artificially engineered metaconcrete with wide bandgap for seismic surface wave manipulation. *Eng. Struct.* **2023**, *276*, 115375. [CrossRef]
34. Guo, J.C.; Li, J.R.; Zhang, Z. Interface design of low-frequency band gap characteristics in stepped hybrid phononic crystals. *Appl. Acoust.* **2021**, *182*, 108209. [CrossRef]
35. Huang, T.T.; Ren, X.; Zeng, Y.; Zhang, Y.; Luo, C.; Zhang, X.Y.; Xie, Y.M. Based on auxetic foam: A novel type of seismic metamaterial for Lamb waves. *Eng. Struct.* **2021**, *246*, 112976. [CrossRef]
36. Geng, Q.; Zhu, S.; Chong, K.P. Issues in design of one-dimensional metamaterials for seismic protection. *Soil Dyn. Earthq. Eng.* **2018**, *107*, 264–278. [CrossRef]
37. Liu, Z.; Qin, K.Q.; Yu, G.L. Partially Embedded Gradient Metabarrier: Broadband Shielding from Seismic Rayleigh Waves at Ultralow Frequencies. *J. Eng. Mech.* **2020**, *146*, 04020032. [CrossRef]
38. Yu, M.; Fang, X.; Yu, D.L.; Wen, J.H.; Cheng, L. Collision enhanced hyper-damping in nonlinear elastic metamaterial. *Chin. Phys. B* **2022**, *31*, 064303. [CrossRef]
39. Yan, Y.; Cheng, Z.; Menq, F.; Mo, Y.L.; Tang, Y.; Shi, Z. Three dimensional periodic foundations for base seismic isolation. *Smart Mater. Struct.* **2015**, *24*, 075006. [CrossRef]
40. Palermo, A.; Krödel, S.; Marzani, A.; Daraio, C. Engineered metabarrier as shield from seismic surface waves. *Sci. Rep.* **2016**, *6*, 39356. [CrossRef]
41. Wang, H.C.; Sun, W.; Sun, W.F.; Ren, Y.; Zhou, Y.Q.; Qian, Q.J.; Kumar, A. A novel tool condition monitoring based on Gramian angular field and comparative learning. *Int. J. Hydromechatron.* **2023**, *6*, 93–107. [CrossRef]
42. Purohit, J.; Dave, R. Leveraging Deep Learning Techniques to Obtain Efficacious Segmentation Results. *Arch. Adv. Eng. Sci.* **2023**, *1*, 11–26. [CrossRef]
43. Gaur, H.; Khidhir, B.A.; Manchiryal, R.K. Solution of structural mechanics problems by machine learning. *Int. J. Hydromechatron.* **2022**, *5*, 22–43. [CrossRef]

44. Liu, B.; Lu, W.Z. Surrogate models in machine learning for computational stochastic multi-scale modeling in composite materials design. *Int. J. Hydromechatron.* **2022**, *5*, 336–365. [CrossRef]
45. Koy, A.; Colak, A.B. The Intraday High-Frequency Trading with Different Data Ranges: A Comparative Study with Artificial Neural Network and Vector Autoregressive Models. *Arch. Adv. Eng. Sci.* **2023**, *2*, 123–133. [CrossRef]
46. Hou, Z.; Assouar, B.M. Modeling of Lamb wave propagation in plate with two-dimensional phononic crystal layer coated on uniform substrate using plane-wave-expansion method. *Phys. Lett. A* **2008**, *372*, 2091–2097. [CrossRef]
47. Kafesaki, M.; Economou, E.N. Multiple-scattering theory for three-dimensional periodic acoustic composites. *Phys. Rev. B* **1999**, *60*, 11993–12001. [CrossRef]
48. Maheshwari, H.K.; Rajagopal, P. Novel locally resonant and widely scalable seismic metamaterials for broadband mitigation of disturbances in the very low frequency range of 0–33 Hz. *Soil Dyn. Earthq. Eng.* **2022**, *161*, 107409. [CrossRef]
49. Psarobas, I.E.; Stefanou, N.; Modinos, A. Scattering of elastic waves by periodic arrays of spherical bodies. *Phys. Rev. B* **2000**, *62*, 278–291. [CrossRef]
50. Sainidou, R.; Stefanou, N.; Psarobas, I.E.; Modinos, A. A layer-multiple-scattering method for phononic crystals and heterostructures of such. *Comput. Phys. Commun.* **2005**, *166*, 197–240. [CrossRef]
51. Fang, X.; Lou, J.; Chen, Y.M.; Wang, J.; Xu, M.; Chuang, K.C. Broadband Rayleigh wave attenuation utilizing an inertant seismic metamaterial. *Int. J. Mech. Sci.* **2023**, *247*, 108182. [CrossRef]
52. Gao, Y.; Wang, L. Ultrawide coupled bandgap in hybrid periodic system with multiple resonators. *J. Appl. Phys.* **2020**, *127*, 204901. [CrossRef]
53. Zeighami, F.; Palermo, A.; Marzani, A. Inertial amplified resonators for tunable metasurfaces. *Meccanica* **2019**, *54*, 2053–2065. [CrossRef]
54. Zeighami, F.; Palermo, A.; Marzani, A. Rayleigh waves in locally resonant metamaterials. *Int. J. Mech. Sci.* **2021**, *195*, 106250. [CrossRef]
55. Oudich, M.; Badreddine Assouar, M. Surface acoustic wave band gaps in a diamond-based two-dimensional locally resonant phononic crystal for high frequency applications. *J. Appl. Phys.* **2012**, *111*, 014504. [CrossRef]
56. Pu, X.B.; Shi, Z.F. A novel method for identifying surface waves in periodic structures. *Soil Dyn. Earthq. Eng.* **2017**, *98*, 67–71. [CrossRef]

Disclaimer/Publisher's Note: The statements, opinions and data contained in all publications are solely those of the individual author(s) and contributor(s) and not of MDPI and/or the editor(s). MDPI and/or the editor(s) disclaim responsibility for any injury to people or property resulting from any ideas, methods, instructions or products referred to in the content.